

# Multistrategy Preparation of Efficient and Stable Environment-Friendly Lead-Based Perovskite Solar Cells

Huan Bi, Gaoyi Han, Mengna Guo, Chao Ding, Hanjun Zou, Qing Shen,\* Shuzi Hayase,\* and Wenjing Hou\*



Cite This: *ACS Appl. Mater. Interfaces* 2022, 14, 35513–35521



Read Online

ACCESS |

Metrics & More



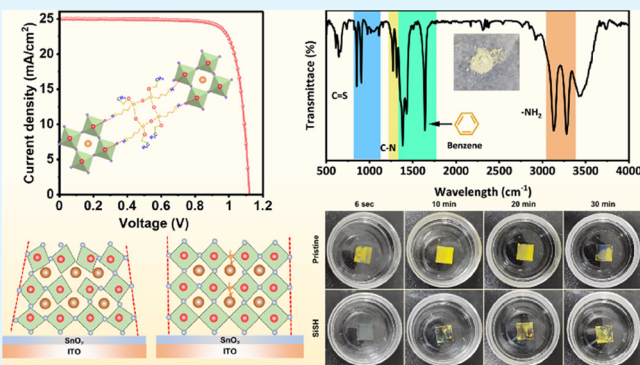
Article Recommendations



Supporting Information

**ABSTRACT:** Perovskite solar cells (PSCs) have achieved huge success in power conversion efficiency (PCE) and stability. However, further improving the PCE of PSCs and stability is still a big challenge. Here, we attempt to improve the PCE and stability of PSCs using a functional additive named 3-mercaptopropyltriethoxysilane (SiSH) in the perovskite antisolvent. It is revealed that SiSH can release the stress in the film, reduce the defects, and inhibit lithium-ion migration and lead leakage. As a result, the target device achieves an efficiency enhancement from 20.80 to 22.42% as compared to the control device. Meanwhile, device stability is ameliorated after SiSH modification. Furthermore, new adsorbents are used to treat the leaked lead to make it comply with safe drinking water standards. This work provides an idea for developing multifunctional antisolvent additives and adsorbents for high PCE, long stability, and environment-friendly Pb-based PSCs.

**KEYWORDS:** lead leakage and recycling, environment-friendly perovskite solar cell, 3-mercaptopropyltriethoxysilane, stress release, lithium-ion migration



## INTRODUCTION

Perovskite solar cells (PSCs) have made great achievement since it was first reported due to their significantly lengthy photoinduced charge carrier diffusion lengths,<sup>1–3</sup> longer carrier lifetime,<sup>4–6</sup> high optical absorption coefficients, and other factors.<sup>7,8</sup> PSCs' power conversion efficiency (PCE) has risen from 3.8% to a certified 25.7%.<sup>9</sup> However, there are still amount of problems that need to be solved such as (1) how to further enhance the PCE of PSCs; (2) how to improve the operational and environmental stability of the PSCs, especially for organic–inorganic PSCs; and (3) how to prevent lead leakage and recover the leaked lead.

The quality of the perovskite film plays a key role in preparing the PSCs with high PCE.<sup>7,10,11</sup> As yet, a lot of methods have been proposed to ameliorate the quality of the perovskite thin film, for example, additive engineering,<sup>5,12,13</sup> buried engineering,<sup>14,15</sup> precursor solvent, and component engineering.<sup>16,17</sup> Besides, the antisolvent engineering<sup>18,19</sup> has been considered one of the most effective ways to enhance the quality of the perovskite film. In addition to finding more suitable and greener antisolvents or mixing antisolvents engineers,<sup>11,18</sup> introducing additives into antisolvents is also an important content of antisolvent engineering. Liu and co-workers applied acetylacetone as an additive of the ethyl acetate antisolvent to treat  $\text{CH}_3\text{NH}_3\text{PbI}_3$  film and found that

acetylacetone indeed can improve the quality of the perovskite films because of the strong chemical interaction between acetylacetone and perovskite film, which can reduce the defect density of the perovskite film.<sup>18</sup> Na and co-workers also obtained a high-performance device with improved film quality and carrier transport by adding a functional additive (2-hydroxyethyl acrylate) in the antisolvent.<sup>20</sup> So far, only a few amounts of works have focused on antisolvent additive engineering,<sup>20–23</sup> but this is a strategy that cannot be ignored to improve the PCE of the PSCs. Therefore, this inspires us to find new and suitable antisolvent additives.

Besides, more and more researchers are drawing their attention to device stability rather than just improving the PCE of the PSCs. Previous studies have proved that the stress in film and interface and  $\text{Li}^+$  migration can influence the device stability by accelerating the decomposition of the perovskite film. Up to now, a lot of studies have been conducted to regulate/release stress<sup>15,24–26</sup> or inhibit  $\text{Li}^+$  migration. Tang

Received: April 6, 2022

Accepted: July 19, 2022

Published: July 30, 2022



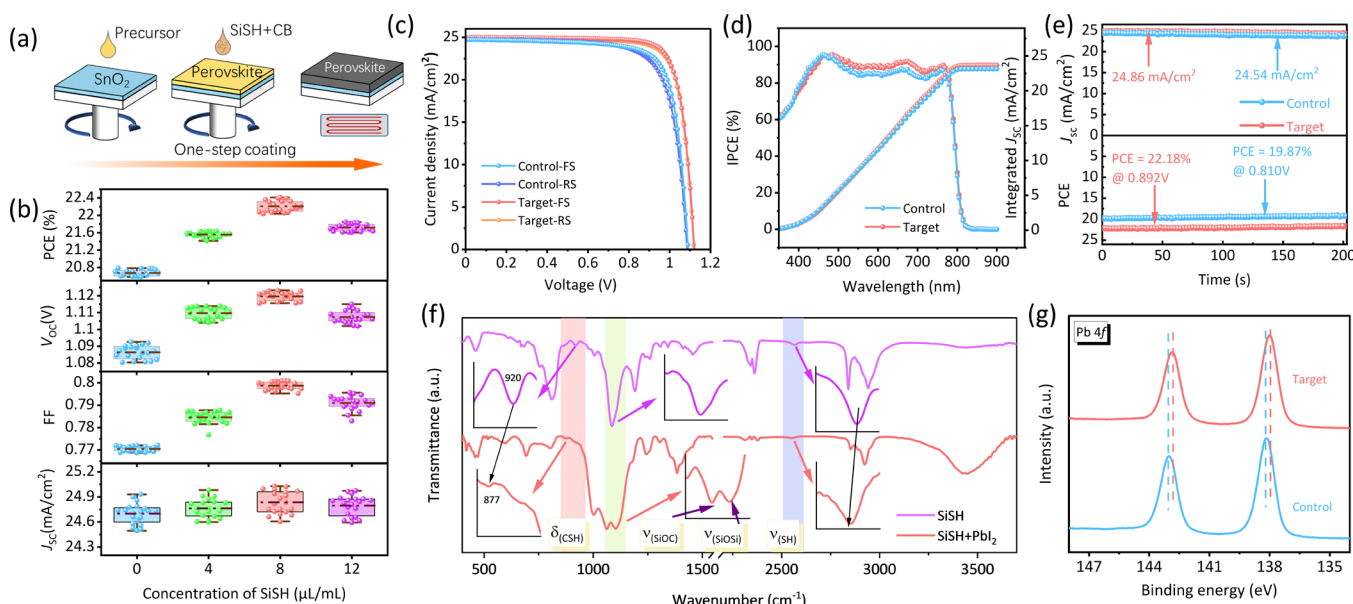


**Figure 1.** (a) Preparation process of the PSCs used in this work. (b) Statistical image of the photovoltaic parameters modified by different concentrations of the SiSH. (c)  $J$ – $V$  curves and (d) corresponding IPCE spectra of the control and target devices. (e) Time dependence of the stabilized current and PCE output of the PSCs with and without SiSH modification. (f) FTIR spectra of the  $\text{PbI}_2$  films without and with SiSH modifications. (g) Pb 4f XPS spectra of the perovskite films without and with SiSH modifications.

and co-workers attempted to insert the  $\text{WS}_2$  interface layer between the electron transport layer (ETL) and perovskite layer to release the perovskite stress due to the matched crystal lattice structure between perovskite,  $\text{SnO}_2$ , and  $\text{WS}_2$ . Meanwhile, the atomically smooth dangling bond-free surface also acts as a lubricant to an adjacent interface.<sup>27</sup> Chen and co-workers studied the effects of different stress states (tensile-strain, strain-free, and compressive-strain) on the PCE and stability of PSCs by using different annealing processes (forward annealing and inverted annealing).<sup>28</sup> Our previous work also tried to use  $\text{KPF}_6$  to release the film stress and improve the environmental stability of the PSCs.<sup>15</sup> On the other hand, lithium-ion migration from the hole transport layer (Spiro-OMeTAD) to the perovskite layer is also harmful to the stability of the device, and up to now, there are some strategies such as top-contact-interface engineering and the hole transport layer additive engineering to solve this issue.<sup>29–31</sup> All the above studies prove that it is a potential and effective strategy to improve the device's stability via releasing/regulating stress or inhibiting lithium-ion migration.

Another concern is that lead leakage comes from PSCs, which could lead to the irreparable pollution of drinking water and soil. A lot of technologies have been proposed to reduce the leaked lead such as superhydrophobic self-assembled monolayers,<sup>32</sup> device packaging, or additive engineering.<sup>33,34</sup> However, because of the complex process and single benefit, these strategies have not been widely promoted. Therefore, how to further prevent the lead leakage and recover the leaked lead is also a top priority.

Here, a multifunctional additive in chlorobenzene (CB), namely, 3-mercaptopropyltriethoxysilane (SiSH) is incorporated to make better the PCE and stability of the PSCs. After SiSH is treated, several functions have been realized synergistically: improving the morphologies of perovskite film by passivating interfacial defects and facilitating perovskite crystallization, enhancing device stability by releasing interfacial stress, inhibiting lithium-ion migration, reducing the

irreversible environment pollution by preventing lead leakage, and achieving lead recovery. In this way, both PCE and stability are enhanced after SiSH introduction. The device modified by SiSH achieves a PCE of 22.42%. After aging in the dark air condition (25 °C, 40~45% RH) for 500 h, the unencapsulated modified device maintains 95% of its initial PCE. In addition, lead leakage was significantly inhibited after SiSH was modified. At the same time, using our synthetic adsorbent, the lead content is controlled in a safe range.

## RESULTS AND DISCUSSION

The structure of the PSCs used in this work was ITO/ $\text{SnO}_2$ / $\text{Rb}_{0.02}(\text{FA}_{0.95}\text{Cs}_{0.05})_{0.98}\text{PbI}_{2.91}\text{Br}_{0.03}\text{Cl}_{0.06}$ /Spiro-OMeTAD/Ag, and the corresponding preparation process is displayed in Figure 1a, where SiSH was introduced into CB to prepare the thin film. Because SiSH molecules contain some functional groups, it is expected to achieve multiple functions by introducing the SiSH into perovskite film, and the structure of SiSH is exhibited in Figure S1. First, sulphydryl (–SH) is expected to passivate the undercoordinated  $\text{Pb}^{2+}$  defects from perovskite film by the coordination interaction. Second, siloxanes have been widely demonstrated to have strong hydrophobics, which are expected to improve the stability of the PSCs. Finally, after introducing SiSH with a flexible chain into perovskite films, it is expected to release the stress in the perovskite films. All in all, multiple functions are anticipated to be achieved through the modification of SiSH molecules for perovskite film.

The photovoltaic performances of the PSCs with different concentrations of SiSH modifications are shown in Figure 1b and Table S1. The result showed that the PCE of PSCs was increased with the concentration of SiSH increased, and the best performance of the PSCs was obtained when the concentration of 8 μL/mL of the SiSH was introduced into CB. Figure 1c exhibits the  $J$ – $V$  curves of control and target devices measured in reverse scan (RS) and forward scan (FS) under simulated AM 1.5G one sun illumination of 100 mW/cm<sup>2</sup>. The open-

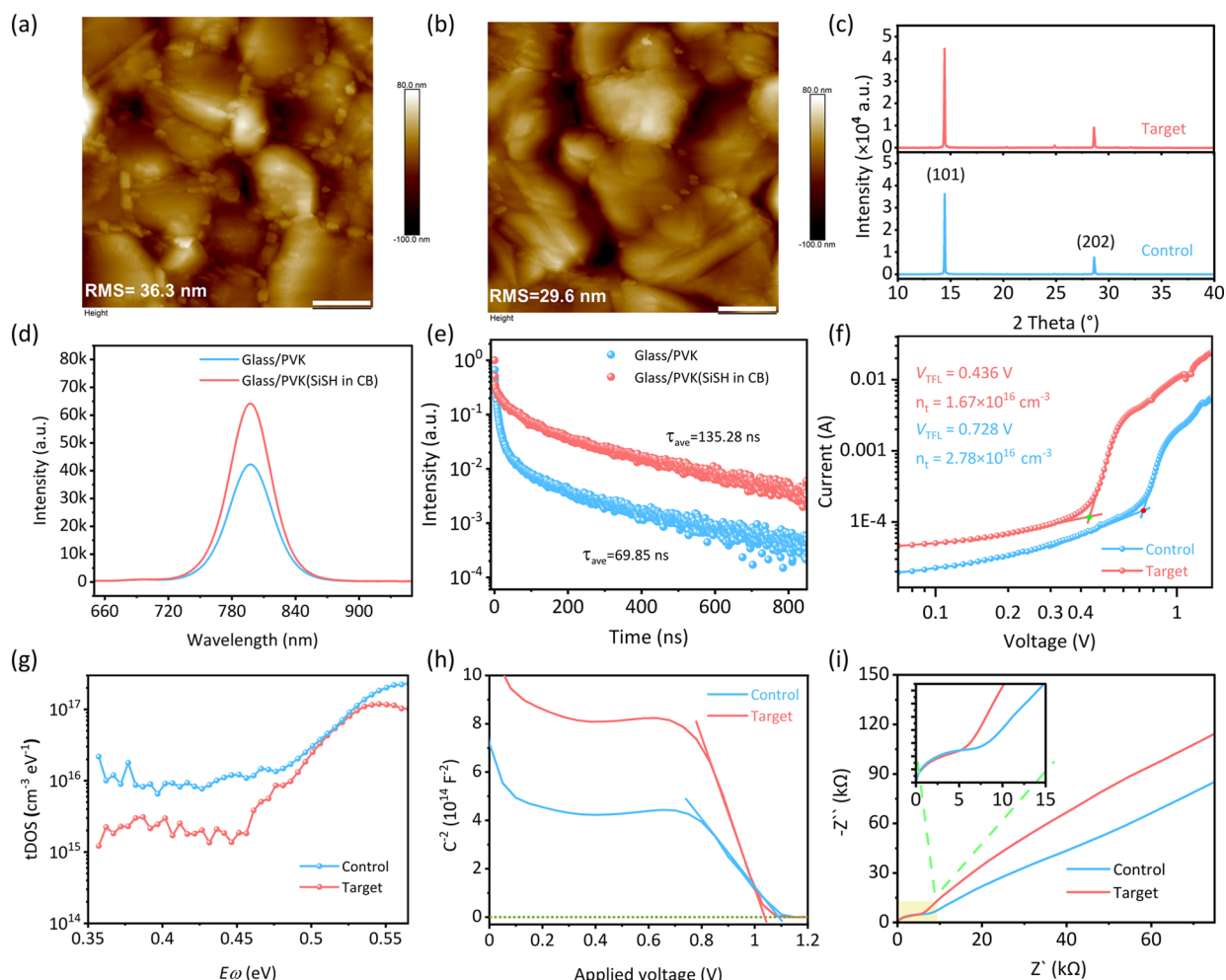


**Figure 2.** AFM topography images of perovskite thin film treated with (a) CB and (b) SiSH + CB. (c) XRD patterns of perovskite film treated with or without SiSH. (d) PL and (e) TRPL of the perovskite film without or with SiSH modification and deposited on glass. (f) Dark  $I-V$  curves with the structure of ITO/control or target perovskite film/Au. (g) TAS, (h) Mott–Schottky plot, and (i) Nyquist plots of the PSCs without or with SiSH treatment.

circuit voltage ( $V_{OC}$ ) and fill factor (FF) were increased significantly from 1.09 V and 77.2% (control device) to 1.12 V and 80.1% (target device) after SiSH was introduced, and the average  $V_{OC}$  and FF increased from 1.09 V and 77.1% (control device) to 1.12 V and 79.8% (target device), respectively. Finally, a high PCE of target PSCs (22.42%) was obtained compared with the control device (20.80%), which is very competitive (see Supplementary Table S2). Figure 1d shows the incident photon-to-current conversion efficiency (IPCE) spectra of the PSCs introduced or not introduced SiSH. The integrated current density of the device can obtain from IPCE and is exhibited in Figure 1d. As we can see, the control device shows a  $J_{SC}$  of 23.14 mA/cm $^2$  while the target is 23.65 mA/cm $^2$ , which echoes with that obtained from  $J-V$  curves. Figure 1e shows the stable output current density and PCE of the devices with or without SiSH introduced in CB at the maximum power point with the bias of 0.810 and 0.892 V, respectively. The SiSH-modified device exhibited a higher current density of 24.86 mA/cm $^2$  and PCE of 22.18%, while those of the control device were 24.54 mA/cm $^2$  and 19.87%, respectively.

To explain the dependence of photovoltaic performance on SiSH, Fourier transform infrared spectroscopy (FTIR) and X-ray photoelectron spectroscopy (XPS) measurements were

carried out. As displayed in Figure 1f, where the vibration peaks of C–S–H in SiSH are located at 920 cm $^{-1}$ <sup>35,36</sup> after mixing with PbI $_2$ , the peaks shifted to 877 cm $^{-1}$ , which indicated that there is a strong chemical interaction between –SH and Pb $^{2+}$ . Furthermore, the stretching vibration peaks of –SH at 2561 cm $^{-1}$  also showed that a shift after PbI $_2$  was introduced into SiSH.<sup>35</sup> In addition, as an effective technology, XPS is often used to characterize the chemical interactions between elements. As exhibited in Figure S2, strong signals belonging to Si 2p could be observed in the target film while they did not appear in the control film, which indicated that there is SiSH existing in the perovskite thin film. Pb 4f was further measured to explore the chemical interaction between SiSH and Pb $^{2+}$ . As revealed in Figure 1g, a definite shift arose after SiSH was introduced into CB during the preparation process of the perovskite thin film (from 138.16 and 143.05 eV for the control film to 137.99 and 142.83 eV for the target film). This is consistent with the FTIR results, indicating that there is indeed a strong chemical interaction between SiSH and Pb $^{2+}$ . In addition, we were surprised to find that after mixing the SiSH and PbI $_2$ , the stretching vibration peaks of Si–O–C located on 1086 cm $^{-1}$  were split into two peaks (1062 and 1108 cm $^{-1}$ ) (Figure 1f),<sup>37,38</sup> where the peak at 1108 cm $^{-1}$  was attributed to the stretching vibration peaks of Si–O–Si,<sup>39</sup>

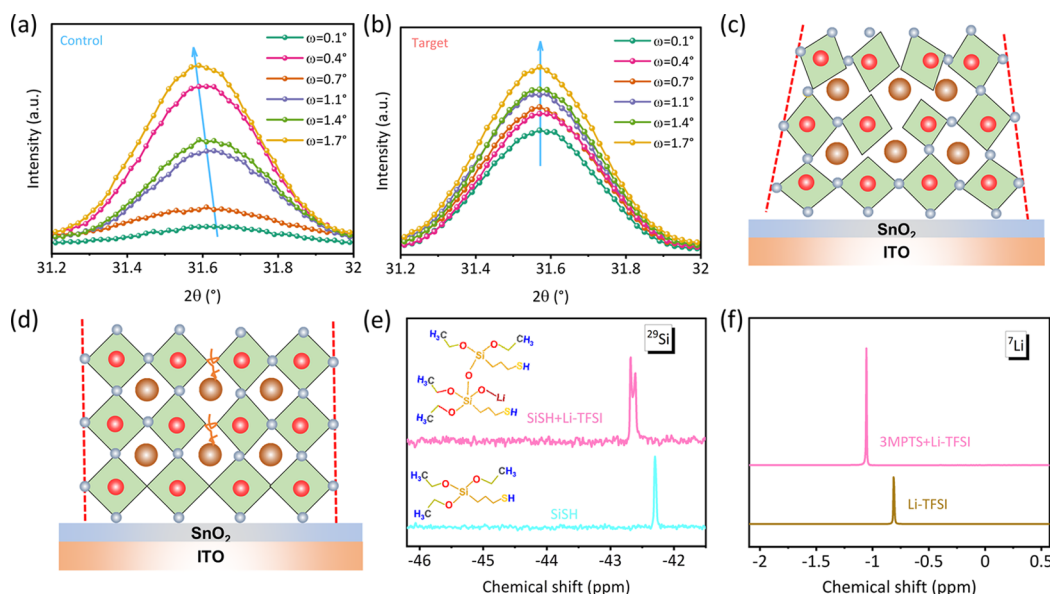


**Figure 3.** GIXRD patterns of the perovskite films (a) without or (b) with SiSH treated. Schematic illustration of the residual stress of the perovskite films (c) without or (d) with SiSH treated. (e) <sup>29</sup>Si and (f) <sup>7</sup>Li NMR of SiSH and Li-TFSI dissolved in DMSO-d<sub>6</sub>.

indicating the formation of the cross-linked network. According to Figure 1f, g, a distribution diagram of SiSH in perovskite films was proposed. As displayed in Figure S3, the strong chemical interaction between –SH and Pb<sup>2+</sup> defect is expected to passivate the under-coordination Pb<sup>2+</sup> defect because of the existence of lone-pair electrons in –SH, which causes the shift of the XPS peak of Pb 4f to the lower binding energy and the corresponding FTIR verb peaks also shifted (Figure 1f, g). At the same time, the formation of the Si–O–Si cross-linked network also ensures the stability of the crystal structure.<sup>6</sup> Finally, the cross-linked network is expected to protect perovskite films from the erosion of water and oxygen.<sup>6</sup>

Atomic force microscopy (AFM) was employed to reveal the morphology of perovskite films without and with SiSH introduction. As expected, the root mean square (RMS) roughness of the perovskite film was reduced from 36.3 nm of the control film to 29.6 nm of the target film (Figure 2a, b). Meanwhile, top-view scanning electron microscopy (SEM) images show that the size of the grain was increased, and the hole of the thin film decreased significantly (Figure S4), which was mainly due to the perovskite crystallization rate being effectively suppressed owing to the strong chemical interaction between Pb<sup>2+</sup> and –SH (in SiSH).<sup>6</sup> Smoother and better coverage film can not only reduce the interfacial nonradiative recombination losses but also improve the light absorption capacity of the film. XRD measurement was implemented to uncover the effect of SiSH treatment on the composition and crystallinity of perovskite thin films. As exhibited in Figure 2c, the composition of the perovskite film was not affected by the SiSH, while the crystallinity of the film increased after SiSH was introduced into CB. Better crystallinity also can lead to high  $J_{SC}$  and  $V_{OC}$ .<sup>6</sup>

The steady-state photoluminescence (PL) and time-resolved photoluminescence (TRPL) spectra were measured with the structure of glass/perovskite to reveal the effect of the SiSH treatment on carrier lifetimes, and the results are shown in Figure 2d, e. As we can see that after introducing SiSH into CB, the PL intensity of the perovskite thin film was increased.

TRPL curves exhibited in Figure 2e can be fitted well using a double-exponential function:<sup>45</sup>

$$I(t) = A_1 e^{(-t/\tau_1)} + A_2 e^{(-t/\tau_2)} \quad (1)$$

where  $\tau_1$  is the fast decay time and  $\tau_2$  stand for the slow decay time. The amplitudes of the fast and slow decay processes are  $A_1$  and  $A_2$ , respectively. The average carrier lifetime ( $\tau_{ave}$ ) can be calculated using the following equation:<sup>40</sup>

$$\tau_{ave} = \frac{A_1 \tau_1^2 + A_2 \tau_2^2}{A_1 \tau_1 + A_2 \tau_2} \quad (2)$$

The fitting parameters are listed in Table S3. As we can see, the film shows a longer carrier lifetime (135.28 ns) after SiSH modification than the bare one (69.85 ns), which suggests that the defect density of the perovskite thin film can be decreased after SiSH was introduced. Dark  $I$ – $V$  curves were further carried out to reveal the defect densities of perovskite film after introducing the SiSH. As illustrated in Figure 2f, three clear regions were observed, including the Ohmic region, the trap-filled limited region, and the SCLC region. It is well known that trap density can be calculated using the following equation:<sup>41,42</sup>

$$n_t = \frac{2\epsilon\epsilon_0 V_{TFL}}{eL^2} \quad (3)$$

where  $\epsilon$  is the dielectric constant of the perovskite,  $e$  is the elementary charge,  $L$  is the thickness film of the perovskite,  $\epsilon_0$  and  $\epsilon$  are the vacuum and practical dielectric constant. The relative dielectric constant was calculated from the capacitance–frequency measurement in the range of 0.1 Hz to 1 MHz with the structure of ITO/perovskite/Au. As shown in Figure S5,  $\epsilon = 51.68$  was obtained when the frequency is 10 kHz.<sup>43</sup> The  $V_{TFL}$  of the device without or with SiSH treatment was 0.728 and 0.436 V, respectively. Also, the corresponding trap densities were decreased from  $2.78 \times 10^{16} \text{ cm}^{-3}$  to  $1.67 \times 10^{16} \text{ cm}^{-3}$ . Improved crystallization and increased grain size are some of the main reasons for the decreased trap density. Besides, the stronger chemical interaction between –SH and

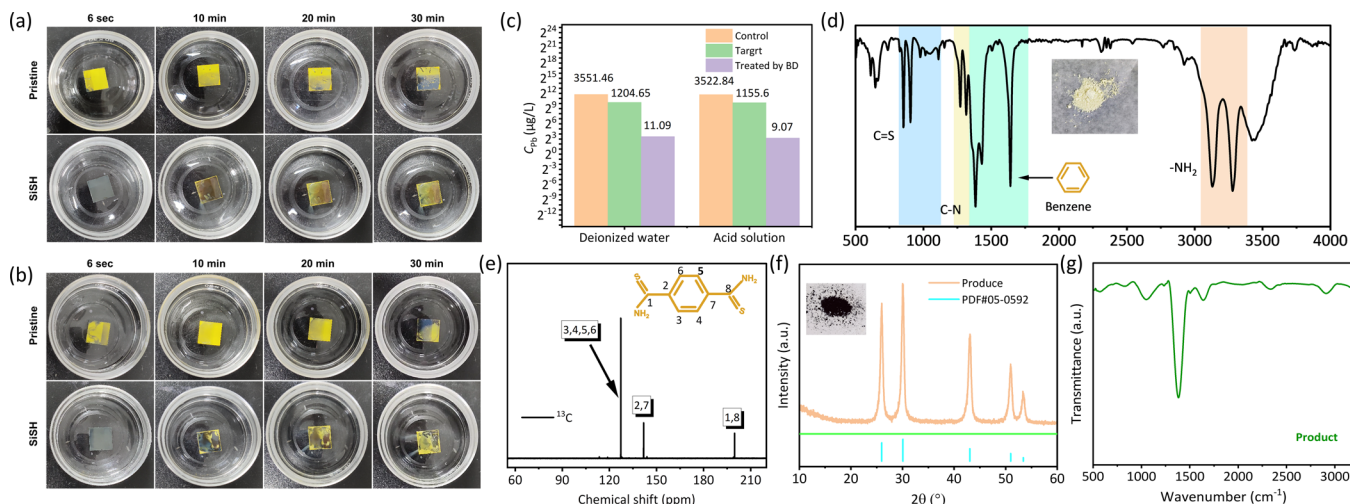


**Figure 4.** Immersing test on the control and target devices using (a) deionized water and (b) simulated acidic rain conditions. (c) Pb concentration under different conditions was measured by ICP-MS. (d) FTIR and (e) <sup>1</sup>H NMR of the BD. (f) XRD and (g) FTIR of the product. The illustration is the picture of PbS.

Pb<sup>2+</sup> and the cross-linked network can also be used to explain the decreased film trap density. Thermal admittance spectroscopy (TAS) measurement was used to analyze the trap density of states (*t*DOS) in energy space for the control and target devices, and the corresponding calculation is displayed in *Supplementary Note 1*. As shown in *Figure 2g*, generally, the energy level from 0.35 to 0.4 eV is defined as shallow trap states, while the energy level from 0.4 to 0.55 eV is attributed to deep trap states.<sup>44,45</sup> After introducing SiSH into CB, both the shallow and deep trap state density can be reduced. PL, TRPL, and TAS results proved that SiSH can effectively passivate the defects at the films and interface and suppress trap-assisted nonradiative recombination correspondingly, which should be related to the increased *V<sub>OC</sub>* and FF. *Figure 2h* shows the Mott–Schottky curves for the control and target devices to reveal the change of the built-in potentials (*V<sub>bi</sub>*). The control device shows a *V<sub>bi</sub>* of 1.038 V while the target device shows a much higher *V<sub>bi</sub>* of 1.089 V, which helps to facilitate carrier transport.<sup>15,40</sup> The Nyquist plots for the control and target devices shown in *Figure 2i* were assessed at the frequency ranging from 1 MHz to 1 Hz with a bias of 0 V under dark conditions. Usually, the high-frequency region is considered to be related to charge-transfer resistance (*R<sub>ct</sub>*), and the low-frequency region is associated with recombination resistance (*R<sub>rec</sub>*).<sup>46,47</sup> On the one hand, the increased *R<sub>rec</sub>* for target devices could be attributed to reducing the defect density and increased carrier lifetime. On the other hand, the reduced *R<sub>ct</sub>* could impinge improved crystallinity and enhanced crystal size. It once more suggests that the SiSH leads to more unencumbered carrier transportation as well as effectively reduced nonradiative recombination losses.

As mentioned before, residual stress was detrimental to device performance because the structure of the perovskite film could be destroyed. The depth-dependent grazing incident X-ray diffraction (GIXRD) as an effective technology was employed to proclaim the stress in the thin film.<sup>26</sup> Here, a serious incident angle ( $\omega$ ) was adopted to reveal the stress distribution in the thin film from  $0.1^\circ$  to  $1.7^\circ$ . Generally, a peak at a high diffraction angle always has a high multiplicative factor and is less affected by the heat movement of the molecule, so the (012) plane at  $31.6^\circ$  was chosen for further

study.<sup>28</sup> As presented in *Figure 3a*, with the increase in the  $\omega$ , the peak position of the control film was shifted to a lower  $2\theta$  angle, while the target thin film has not shifted (*Figure 3b*). According to the Bragg's Law,

$$n\lambda = 2ds\sin\theta \quad (4)$$

where  $\theta$  is the diffraction angle,  $n$  is the diffraction series, and  $d$  stands for interplanar spacing. When the diffraction peak shifted toward a lower  $2\theta$  angle, a large interplanar spacing would generate, indicating the possible lattice expansion and associated stress. The corresponding model is shown in *Figure 3c, d*. The release of stress is mainly due to the softness of SiSH. SiSH could enter the perovskite thin film with CB and stay at the grain boundary, which plays the role of "lubricant," as shown in *Figure S3*. Stress-released thin film has a more stable structure and can effectively prevent the invasion of water and reduce the nonradiative recombination of the thin film. As is known to all, Li<sup>+</sup> migration is also harmful to the stability of the device. Here, <sup>29</sup>Si and <sup>7</sup>Li NMR were employed to uncover the chemical interaction between Li<sup>+</sup> and SiSH (*Figure 3e, f*). After mixing Li<sup>+</sup> and SiSH, the typical NMR of <sup>29</sup>Si and <sup>7</sup>Li has a significant shift, which indicates that a strong chemical interaction indeed exists between Li<sup>+</sup> and SiSH and could inhibit the migration of Li<sup>+</sup> (the illustration of *Figure 3e* shows this potential chemical interaction).<sup>39</sup> Such interaction is also expected to improve the stability of the device.

Inspired by the positive effect of SiSH on defect passivation, stress release, and Li<sup>+</sup> migration inhibition, the long-term stability of the unsealed devices without and with SiSH was recorded. Usually, silver (Ag) is substituted by gold (Au) to explore the stability of the device because Ag reacts with I to form AgI easily, which is harmful to the stability of the device.<sup>15,40</sup> However, previous work demonstrated that –SH and Ag could form a strong chemical interaction.<sup>32</sup> As shown in *Figure S6*, Ag was directly vapor-deposited on perovskite film. When placed for a while, silver iodide (AgI) formed in the control film while the target film did not obvious. Here, the structure with ITO/SnO<sub>2</sub>/perovskite/Spiro-OMeTAD/Ag was adopted to explore the device stability with or without SiSH modification. *Figure S7* presents the humidity stability of the unencapsulated control and target device with 40~45% relative

humidity at 25 °C in the dark for 500 h. The control device only maintains 60% of its original PCE while the target device still maintains 95%. Figure S8 displays the control and target PSCs aged under one sun illumination at room temperature to evaluate the light stability of the devices. After 100 h, the PCE of the control device was degraded by 13%, while the PCE of the device with SiSH modification was degraded only by 3%. Improved device stability can be due to improved thin film properties and inhibited Li-ion and Ag-ion migration, which strongly suggested that SiSH indeed is an effective antisolvent additive.

For a long time, Pb-based PSCs have been always criticized by scientists because of the occurrence of lead leakage, which is contrary to the environment-friendly development advocated all the time. This prompted us to evaluate the lead leakage of control and target film under different conditions. As displayed in Figure 4a, Videos S1 and S2, we put the film into deionized water for 30 min to evaluate the lead leakage. After 30 min, part of the target film was still brown while part of the control film was dissolved, which means that a lot of Pb<sup>2+</sup> in the control film has entered into deionized water. The result proved that the SiSH can effectively prevent Pb<sup>2+</sup> from dissolving in deionized water because of the strong chemical interaction. In addition, considering the commercialization process of PSCs, it is essential to use them in environmental conditions. Therefore, some extreme weather must be considered. Here, we simulated acidic rain conditions to evaluate the advantages of SiSH (Figure 4b, Videos S3 and S4). As exhibited in Figure 4b, after immersing in deionized water with a pH of 5.7 for 30 min, part of the control film was dissolved in water while the target film is still not dissolved. The inductively coupled plasma mass spectrometry (ICP-MS) measurements were used to further characterize the concentration of Pb<sup>2+</sup> in deionized water whether under deionized water or acidic rain conditions. As exhibited in Figure 4c, because of the SiSH, the target film shows less lead leakage (1204.65 µg/L in the deionized water and 1155.60 µg/L in the acidic rain) while the control film shows a more serious lead leakage (3551.46 µg/L in the deionized water and 3522.84 µg/L in the acidic rain). The significantly suppressed lead leakage cannot only be attributed to strong chemical interactions between Pb<sup>2+</sup> and SiSH but also the superhydrophobicity of the cross-linked network of SiSH.

Although a sea of Pb<sup>2+</sup> has been prevented from dissolving in deionized water, there is still a large disparity with drinking water. According to the <standards for drinking water quality> established by some countries, generally, the concentration of the Pb<sup>2+</sup> in water should be lower than 10 µg/L;<sup>48,49</sup> hence, some other strategies should be developed to further reduce the concentration of Pb<sup>2+</sup> in water. We synthesized an adsorbent called benzene-1,4-dithiocarboxamide (BD), the detailed synthesis of which is shown in the Experimental Section and Scheme 1. In Figure 4d, e, FTIR and <sup>1</sup>H NMR spectra were employed to characterize the molecular structure. Typical groups such as C=S, C—N, —NH<sub>2</sub>, and benzenoid can be observed. Meanwhile, <sup>1</sup>H NMR further proved that the

BD is successfully synthesized. Then, BD was used to further reduce the concentration of Pb<sup>2+</sup> in water. After adding the BD to the leachate for the immersion test, there is some black precipitation formed (Video S5). As shown in Figure 4f, g, XRD and FTIR were applied to prove what the product is. The XRD results of the product are in good agreement with those of PbS (PDF card: 05-0592). FTIR also displayed the typical Pb—S vibration peak. Therefore, here, lead recycling was realized through BD. Meanwhile, as shown in Figure 4c, after treatment by BD, the Pb<sup>2+</sup> concentration in deionized water and simulated acidic rain conditions reduced to 11.09 and 9.07, respectively, which is close to the standards for drinking water quality of Japan and China.<sup>49</sup>

## CONCLUSIONS

In summary, a multifunctional antisolvent additive (SiSH) was proposed to both improve the PCE and stability of the PSCs. FTIR and XPS results suggested that a strong chemical interaction exists between SiSH and perovskite thin film, which can reduce the undercoordinated Pb defect and consolidate the structure of perovskite films. Furthermore, notorious Li-ion migration and film stress were also improved. The target device exhibited a high PCE of 22.42% and excellent humidity stability. Finally, a new type of Pb adsorbent was synthesized and used to reduce the content of Pb in the solution to reduce the pollution of heavy metals to the environment. This work not only guides the preparation of efficient, stable, and environment-friendly perovskite but also provides a new strategy for Pb recovery. We believe that this work could be widely used in the field of perovskite solar cells in the future.

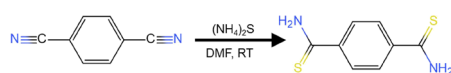
## EXPERIMENTAL SECTION

**Materials.** The SnO<sub>2</sub> colloid precursor with 15% in H<sub>2</sub>O colloidal dispersion was brought from Thermo Scientific. Methylamine hydrochloride (MACl, 99.5%), lead(II) chloride (PbCl<sub>2</sub>, 99.99%), and lead(II) iodide (PbI<sub>2</sub>, 99.99%) were obtained from Xi'an Polymer Light Technology Corp and used directly. Formamidine hydroiodide (FAI, 99.9%), 4-*tert*-butyl pyridine (tBP, 99%), Spiro-OMeTAD (99.86%), Li-TFSI (99%), and lead(II) bromide (PbBr<sub>2</sub>, 99.9%) were all purchased from Advanced Electron Technology CO., Ltd. and used without further purification. Cesium iodide (CsI, 99.99%) and Rubidium iodide (RbI) were obtained from Aladdin. Sigma Aldrich supplied *N,N*-dimethylformamide (DMF, 99.8%), chlorobenzene (CB, 99.8%), and dimethyl sulfoxide (DMSO, 99.9%) and used directly. 3-Mercaptopropyltriethoxysilane (SiSH, 97%) was brought from Macklin.

**Synthesis of Benzene-1,4-Dithiocarboxamide.** To a stirred solution of 1,4-dicyanobenzene (purchased from Macklin, 98%) in DMF was added ammonium sulfide (purchased from Macklin, 14% in H<sub>2</sub>O) (1:2, mol:mol) and was stirred at room temperature for 20 h. The solution was then poured onto ethanol anhydrous for recrystallization. After repeating the above steps several times, the obtained product is filtered to obtain a yellow solid (BD). The yellow solid can be used after vacuum drying. The synthetic route can be seen in the following.

**Device Fabrication.** ITO glasses (7–9 Ω per square) were cleaned using detergent water and ethanol for 20 min. After being dried with nitrogen, the ITO was exposed to ultraviolet ozone for 30 min (UVO). The SnO<sub>2</sub> solution was mixed with deionized water at a volume ratio of 1:3 to create the SnO<sub>2</sub> colloidal solution. Spin-coating diluted SnO<sub>2</sub> colloidal solution onto ITO substrates took place for 30 s at a speed of 3000 rpm, and the SnO<sub>2</sub> film was then annealed for 30 min at 150 °C. It underwent a 20 min UVO treatment after cooling to room temperature. The substrates were then put in a glovebox filled with argon to start the perovskite deposition process. PbI<sub>2</sub> (682.7 mg), PbBr<sub>2</sub> (8.5 mg), RbI (6.6 mg), PbCl<sub>2</sub> (12.7 mg), CsI (19.7 mg),

**Scheme 1. Synthetic Route of Benzene-1,4-Dithiocarboxamide at Room Temperature (RT)**



FAI (248.2 mg), and MACl (35 mg, additive) were dissolved in DMSO/DMF (1/4, v/v) to create the perovskite solution. The perovskite film was fabricated using a sequential spin-coating technique at 4000 rpm for 30 s, followed by the application of 80 L of CB antisolvent for 16 s before the process was stopped. The film was then annealed at 130 °C for 28 min while SiSH was dissolved in CB at various concentrations as an antisolvent additive (0, 4, 8, and 12 L/mL). After that, perovskite thin film was placed in the environment with a relative humidity of 20~25% for 10 min. The Spiro-OMeTAD solution consisted of 72.3 mg of Spiro-OMeTAD, 28.8 L of 4-*tert*-butyl pyridine (tBP), and 17.5 L of Li-TFSI stock solution (520 mg of Li-TFSI in 1 mL of acetonitrile) in 1 mL of CB. The next step was to spin-coat the Spiro-OMeTAD solution onto the perovskite films at 4000 rpm for 30 s to make the hole transport layer. Finally, a shadow mask was used to thermally evaporate about 100 nm of Ag from the top of the Spiro-OMeTAD film at a vacuum of  $3 \times 10^{-3}$  Pa.

**Characterization.** XRD and GIXRD patterns were collected using a PANalytical Empyrean diffractometer equipped. *J-V* curves were measured (FS: -0.01 ~ 1.15 V; RS: 1.15 ~ -0.01 V; scan rate: 120 mV/s) using a solar simulator equipped with a 150 W xenon lamp and a Keithley 2400 source meter. The area of the device was strictly controlled to 0.09 cm<sup>2</sup> by using a black metal mask. The IPCE measurement was conducted on a Zahner electrochemical workstation. UV-vis absorption measurement was tested by Agilent 8453 UV-Vis G1103A. SEM images were observed using JSM-7800F. The FTIR spectra were recorded with a Nicolet iS50 Infrared Fourier transform microscope by Tensor27, BRUKER. PL and TRPL spectra were measured using a 485 nm pulse laser (PDL808, PicoQuant, 90 ps) with a repetition rate of 1 MHz. The Pb concentration in the water was detected using an ICP-MS instrument NexION 350. AFM measurement was performed on Bruker MultiMode 8-HR in tapping mode. Electrochemical impedance spectroscopy was measured using an electrochemical workstation (Chenhua, shanghai). The X-ray photoelectron spectrometer (Thermo Fischer, ESCALAB 250Xi) was used in this work. In the analysis room, the vacuum is  $8 \times 10^{-10}$  Pa, the excitation source is Al K $\alpha$  ray ( $h\nu = 1486.6$  eV), and the working voltage is 12.5 kV. Charge correction was carried out according to the energy standard of C 1s = 284.80 eV. TAS measurements were performed using an electrochemical workstation (CHI 660e). NMR was measured by BRUKER AVANCE III with 600 MHz. The practical dielectric constant was measured using an electrochemical workstation (Zahner) with the structure of ITO/perovskite/Au.

## ASSOCIATED CONTENT

### Supporting Information

The Supporting Information is available free of charge at <https://pubs.acs.org/doi/10.1021/acsami.2c06032>.

Structure of the SiSH, mechanism of crystallization modulation and defect passivation, SEM image and the dielectric constant of the perovskite film, XRD measurement of the perovskite film covered with Ag, test of humidity stability and light stability, summary of the photovoltaic parameters of the devices treated with different concentrations of the SiSH, TRPL fitting results, and summarized additive strategies to obtain a high PCE and environment-friendly device ([PDF](#))

Video: Film is soaked in different conditions (acid rain and water) and the process of lead recycling ([MP4](#))

Video of water target film soaked in water ([MP4](#))

Video of control film soaked in acid rain ([MP4](#))

Video of target film soaked in acid rain ([MP4](#))

Video of Pb recovery ([MP4](#))

## AUTHOR INFORMATION

### Corresponding Authors

**Qing Shen** – Graduate School of Informatics and Engineering, The University of Electro-Communication, Tokyo 182-8585, Japan;  [orcid.org/0000-0001-8359-3275](https://orcid.org/0000-0001-8359-3275); Email: [shen@pc.uec.ac.jp](mailto:shen@pc.uec.ac.jp)

**Shuzi Hayase** – Graduate School of Informatics and Engineering, The University of Electro-Communication, Tokyo 182-8585, Japan;  [orcid.org/0000-0001-8192-5336](https://orcid.org/0000-0001-8192-5336); Email: [hayase@uec.ac.jp](mailto:hayase@uec.ac.jp)

**Wenjing Hou** – Institute of Molecular Science, Key Laboratory of Materials for Energy Conversion and Storage of Shanxi Province, Shanxi University, Taiyuan 030006, P. R. China; Email: [houwenjing@sxu.edu.cn](mailto:houwenjing@sxu.edu.cn)

### Authors

**Huan Bi** – Graduate School of Informatics and Engineering, The University of Electro-Communication, Tokyo 182-8585, Japan; Institute of Molecular Science, Key Laboratory of Materials for Energy Conversion and Storage of Shanxi Province, Shanxi University, Taiyuan 030006, P. R. China;  [orcid.org/0000-0001-7680-9816](https://orcid.org/0000-0001-7680-9816)

**Gaoyi Han** – Institute of Molecular Science, Key Laboratory of Materials for Energy Conversion and Storage of Shanxi Province, Shanxi University, Taiyuan 030006, P. R. China;  [orcid.org/0000-0002-7019-3392](https://orcid.org/0000-0002-7019-3392)

**Mengna Guo** – Institute of Molecular Science, Key Laboratory of Materials for Energy Conversion and Storage of Shanxi Province, Shanxi University, Taiyuan 030006, P. R. China

**Chao Ding** – Graduate School of Informatics and Engineering, The University of Electro-Communication, Tokyo 182-8585, Japan

**Hanjun Zou** – Analytical and Testing Center, Chongqing University, Chongqing 401331, P. R. China

Complete contact information is available at:

<https://pubs.acs.org/10.1021/acsami.2c06032>

### Author Contributions

H.B.: Conceptualization; validation; investigation; writing—original draft; writing—review and editing; G.H.: Validation; resources; M.G.: Validation; C.D.: Resources; H.Z.: Resources; Q.S.: Conceptualization; resources; writing—review and editing; supervision; S.H.: Resources; funding acquisition; W.H.: Conceptualization; resources; writing—review and editing; supervision; funding acquisition; supervision.

### Notes

The authors declare no competing financial interest.

## ACKNOWLEDGMENTS

This work was financially supported by the National Natural Science Foundation of China (U21A20172, 61804091, and U21A6004), Scientific and Technological Innovation Programs of Higher Education Institutions in Shanxi (2020L0002, 2020L0032), and the Natural Science Foundation of Shanxi Province under Grant (201901D211127, 201901D211146), and the Program of State Key Laboratory of Quantum Optics and Quantum Optics Devices (No: KF201910). We are grateful for the Scientific Research Start-up Funds of Shanxi University, and the Hundred Talents Plan of Shanxi Province. This research was partly supported by the Japan Science and Technology Agency (JST) Mirai program (JPMJMI17EA). We

also would like to thank Shiyanjia Lab ([www.shiyanjia.com](http://www.shiyanjia.com)) for the support of the XPS test.

## ■ REFERENCES

- (1) Ding, X.; Wang, H.; Chen, C.; Li, H.; Tian, Y.; Li, Q.; Wu, C.; Ding, L.; Yang, X.; Cheng, M. Passivation Functionalized Phenothiazine-Based Hole Transport Material for Highly Efficient Perovskite Solar Cell With Efficiency Exceeding 22%. *Chem. Eng. J.* **2021**, *410*, No. 128328.
- (2) Zhang, F.; Huang, Q.; Song, J.; Hayase, S.; Qu, J.; Shen, Q. A New Strategy for Increasing the Efficiency of Inverted Perovskite Solar Cells to More than 21%: High-Humidity Induced Self-Passivation of Perovskite Films. *Sol. RRL* **2020**, *4*, No. 2000149.
- (3) Kim, H. S.; Lee, C. R.; Im, J. H.; Lee, K. B.; Moehl, T.; Marchioro, A.; Moon, S. J.; Humphry-Baker, R.; Yum, J. H.; Moser, J. E.; Gratzel, M.; Park, N. G. Lead Iodide Perovskite Sensitized All-Solid-State Submicron Thin Film Mesoscopic Solar Cell with Efficiency Exceeding 9%. *Sci. Rep.* **2012**, *2*, 591.
- (4) Bi, H.; Guo, Y.; Guo, M. N.; Ding, C.; Hayase, S.; Mou, T.; Shen, Q.; Han, G. Y.; Hou, W. J. Highly Efficient and Low Hysteresis Methylammonium-free Perovskite Solar Cells based on Multifunctional Oteracil Potassium Interface Modification. *Chem. Eng. J.* **2022**, *439*, No. 135671.
- (5) Zhang, F.; Zhu, K. Additive Engineering for Efficient and Stable Perovskite Solar Cells. *Adv. Energy Mater.* **2020**, *10*, No. 1902579.
- (6) Xie, L.; Chen, J.; Vashishtha, P.; Zhao, X.; Shin, G. S.; Mhaisalkar, S. G.; Park, N.-G. Importance of Functional Groups in Cross-Linking Methoxysilane Additives for High-Efficiency and Stable Perovskite Solar Cells. *ACS Energy Lett.* **2019**, *4*, 2192–2200.
- (7) Kim, J. Y.; Lee, J. W.; Jung, H. S.; Shin, H.; Park, N. G. High-Efficiency Perovskite Solar Cells. *Chem. Rev.* **2020**, *120*, 7867–7918.
- (8) Luo, D. Y.; Su, R.; Zhang, W.; Gong, Q. H.; Zhu, R. Minimizing Non-radiative Recombination Losses in Perovskite Solar Cells. *Nat. Rev. Mater.* **2020**, *5*, 44–60.
- (9) NREL Best research-cell efficiency chart. <https://www.nrel.gov/pv/cell-efficiency.html>.
- (10) Dai, Z. H.; Xie, J. L.; Liu, W. G.; Ge, S. B.; Zhou, S.; Zhu, Y. C. Research Progress in Stability of Perovskite Solar Cells. *Rare Met. Mater. Eng.* **2020**, *49*, 377–384.
- (11) Liu, Z. H.; Ono, L. K.; Qi, Y. B. Additives in Metal Halide Perovskite Films and Their Applications in Solar Cells. *J. Energy Chem.* **2020**, *46*, 215–228.
- (12) Yang, Y.; You, J.; Zhang, J.; Su, H.; Du, X.; Hu, Y.; Xu, T.; Gao, L.; Liu, S. F. Cation Engineering for Effective Defect Passivation to Improve Efficiency and Stability of  $\text{FA}_{0.5}\text{MA}_{0.5}\text{PbI}_3$  Perovskite Solar Cells. *ACS Appl. Energy Mater.* **2021**, *4*, 7654–7660.
- (13) Zhang, F.; Hou, Y. Z.; Wang, S.; Zhang, H. H.; Zhou, F. F.; Hao, Y. Y.; Ye, S.; Cai, H. Z.; Song, J.; Qu, J. L. Solvent-Additive Engineering-Assisted Improvement of Interface Contact for Producing Highly Efficient Inverted Perovskite Solar Cells. *Sol. RRL* **2021**, *5*, No. 2100190.
- (14) Xu, X. J.; Ji, X. Y.; Chen, R.; Ye, F. Y.; Liu, S. J.; Zhang, S.; Chen, W.; Wu, Y. Z.; Zhu, W. H. Improving Contact and Passivation of Buried Interface for High-Efficiency and Large-Area Inverted Perovskite Solar Cells. *Adv. Funct. Mater.* **2022**, *32*, No. 2109968.
- (15) Bi, H.; Liu, B. B.; He, D. M.; Bai, L.; Wang, W. Q.; Zang, Z. G.; Chen, J. Z. Interfacial Defect Passivation and Stress Release by Multifunctional  $\text{KPF}_6$  Modification for Planar Perovskite Solar Cells with Enhanced Efficiency And Stability. *Chem. Eng. J.* **2021**, *418*, No. 129375.
- (16) Lin, Z.; Zhang, W.; Cai, Q.; Xu, X.; Dong, H.; Mu, C.; Zhang, J. P. Precursor Engineering of the Electron Transport Layer for Application in High-Performance Perovskite Solar Cells. *Adv. Sci.* **2021**, *8*, No. e2102845.
- (17) Wei, Q.; Chang, D.; Ye, Z.; Li, X.; Zan, L.; Gao, L.; Fu, F.; Yang, D. Giant Improvement of Performances of Perovskite Solar Cells via Component Engineering. *J. Colloid Interface Sci.* **2021**, *588*, 393–400.
- (18) Li, J.; Hua, X.; Gao, F.; Ren, X.; Zhang, C.; Han, Y.; Li, Y.; Shi, B.; Liu, S. Green Antisolvent Additive Engineering to Improve the Performance of Perovskite Solar Cells. *J. Energy Chem.* **2022**, *66*, 1–8.
- (19) Qiu, L. L.; Dong, L. K.; Mei, D. Q.; Chen, W. H.; Song, L. X.; Wang, J. Q.; Zou, J. C.; Jiang, P. C.; Du, P. F.; Xiong, J. A Simple Fabrication of High Efficiency Planar Perovskite Solar Cells: Controlled Film Growth with Methylammonium Iodide and Green Antisolvent Sec-butyl Alcohol. *J. Mater. Chem. C* **2020**, *8*, 12560–12567.
- (20) Kang, Y.-J.; Kwon, S.-N.; Cho, S.-P.; Seo, Y.-H.; Choi, M.-J.; Kim, S.-S.; Na, S.-I. Antisolvent Additive Engineering Containing Dual-Function Additive for Triple-Cation p-i-n Perovskite Solar Cells with over 20% PCE. *ACS Energy Lett.* **2020**, *5*, 2535–2545.
- (21) Huang, Y.; Wu, S.; Chen, R.; Fang, S.; Zhang, S.; Wang, G.; Chen, W. Efficient Methylamine-Containing Antisolvent Strategy to Fabricate High-Efficiency and Stable  $\text{FA0.85Cs0.15Pb(Br0.15I2.85)}$  Perovskite Solar Cells. *ACS Appl. Mater. Interfaces* **2019**, *11*, 18415–18422.
- (22) Wang, H. P.; Zeng, W. J.; Xia, R. D. Antisolvent Diethyl Ether as Additive to Enhance the Performance of Perovskite Solar Cells. *Thin Solid Films* **2018**, *663*, 9–13.
- (23) Yang, F.; Kamarudin, M. A.; Zhang, P.; Kapil, G.; Ma, T.; Hayase, S. Enhanced Crystallization by Methanol Additive in Antisolvent for Achieving High-Quality  $\text{MAPbI}_3$  Perovskite Films in Humid Atmosphere. *ChemSusChem* **2018**, *11*, 2348–2357.
- (24) Zhang, Z.; Wang, J.; Lang, L.; Dong, Y.; Liang, J.; Zheng, Y.; Wu, X.; Tian, C.; Huang, Y.; Zhou, Z.; Yang, Y.; Wang, L.; Kong, L.; Chen, C.-C. Size-tunable  $\text{MoS}_2$  Nanosheets for Controlling the Crystal Morphology and Residual Stress in Sequentially Deposited Perovskite Solar Cells with over 22.5% Efficiency. *J. Mater. Chem. A* **2022**, *10*, 3605–3617.
- (25) Yang, N.; Zhu, C.; Chen, Y. H.; Zai, H. C.; Wang, C. Y.; Wang, X.; Wang, H.; Ma, S.; Gao, Z. Y.; Wang, X. Y.; Hong, J. W.; Bai, Y.; Zhou, H. P.; Cui, B. B.; Chen, Q. An in Situ Cross-Linked 1D/3D Perovskite Heterostructure Improves the Stability of Hybrid Perovskite Solar Cells for Over 3000 h Operation. *Energy Environ. Sci.* **2020**, *13*, 4344–4352.
- (26) Liu, G.; Zhong, Y.; Mao, H.; Yang, J.; Dai, R.; Hu, X.; Xing, Z.; Sheng, W.; Tan, L.; Chen, Y. Highly Efficient and Stable  $\text{ZnO}$ -based MA-Free Perovskite Solar Cells via Overcoming Interfacial Mismatch and Deprotonation Reaction. *Chem. Eng. J.* **2022**, *431*, No. 134235.
- (27) Zhou, Q.; Duan, J.; Yang, X.; Duan, Y.; Tang, Q. Interfacial Strain Release from the  $\text{WS}_2/\text{CsPbBr}_3$  van der Waals Heterostructure for 1.7 V Voltage All-Inorganic Perovskite Solar Cells. *Angew. Chem., Int. Ed. Engl.* **2020**, *59*, 21997–22001.
- (28) Zhu, C.; Niu, X.; Fu, Y.; Li, N.; Hu, C.; Chen, Y.; He, X.; Na, G.; Liu, P.; Zai, H.; Ge, Y.; Lu, Y.; Ke, X.; Bai, Y.; Yang, S.; Chen, P.; Li, Y.; Sui, M.; Zhang, L.; Zhou, H.; Chen, Q. Strain Engineering in Perovskite Solar Cells and Its Impacts on Carrier Dynamics. *Nat. Commun.* **2019**, *10*, 815.
- (29) Li, B. X.; Zhang, S. Y.; Xia, F.; Huang, Y. L.; Ran, X. Q.; Xia, Y. D.; Chen, Y. H.; Huang, W. Insights into the Hole Transport Properties of LiTFSI-doped Spiro-OMeTAD Films through Impedance Spectroscopy. *J. Appl. Phys.* **2020**, *128*, No. 085501.
- (30) Liu, Y.; Hu, Y. C.; Zhang, X. Y.; Zeng, P.; Li, F. M.; Wang, B.; Yang, Q.; Liu, M. Z. Inhibited Aggregation of Lithium Salt in Spiro-Ometad toward Highly Efficient Perovskite Solar Cells. *Nano Energy* **2020**, *70*, No. 104483.
- (31) Jiang, L. L.; Wang, Z. K.; Li, M.; Li, C. H.; Fang, P. F.; Liao, L. S. Flower-like  $\text{MoS}_2$  Nanocrystals: A Powerful Sorbent of  $\text{Li}^+$  in The Spiro-Ometad Layer for Highly Efficient and Stable Perovskite Solar Cells. *J. Mater. Chem. A* **2019**, *7*, 3655–3663.
- (32) Zhang, H.; Li, K.; Sun, M.; Wang, F. L.; Wang, H.; Jen, A. K. Y. Design of Superhydrophobic Surfaces for Stable Perovskite Solar Cells with Reducing Lead Leakage. *Adv. Energy Mater.* **2021**, *11*, No. 2102281.
- (33) Li, X.; Zhang, F.; Wang, J. X.; Tong, J. H.; Xu, T.; Zhu, K. On-device Lead-absorbing Tapes for Sustainable Perovskite Solar Cells. *Nat. Sustain.* **2021**, *4*, 1038.

- (34) Meng, X.; Hu, X.; Zhang, Y.; Huang, Z.; Xing, Z.; Gong, C.; Rao, L.; Wang, H.; Wang, F.; Hu, T.; Tan, L.; Song, Y.; Chen, Y. A Biomimetic Self-Shield Interface for Flexible Perovskite Solar Cells with Negligible Lead Leakage. *Adv. Funct. Mater.* **2021**, *31*, No. 2106460.
- (35) Li, Y. S.; Wang, Y.; Tran, T.; Perkins, A. Vibrational Spectroscopic Studies of (3-Mercaptopropyl)Trimethoxysilane Sol-Gel and Its Coating. *Spectrochim. Acta, Part A* **2005**, *61*, 3032–3037.
- (36) Chang, T. C.; Wu, K. H. NMR Study of the Polysiloxaneimides Doped with LiCF<sub>3</sub>SO<sub>3</sub>. *Phosphorus, Sulfur Silicon Relat. Elem.* **1997**, *130*, 15–22.
- (37) Nakanabi, K.; Solomon, P. H. Infrared Absorption Spectroscopy; *Emerson Adams Pr Inc.*, 1977.
- (38) Lu, Y.; Deng, Z. *Practical Infrared Spectroscopy*; Publishing House of Electronics Industry: China, 1989.
- (39) Ye, X. M.; Zhang, W. C.; Yang, R. J.; He, J. Y.; Li, J. R.; Zhao, F. Q. Facile Synthesis of Lithium Containing Polyhedral Oligomeric Phenyl Silsesquioxane and Its Superior Performance in Transparency, Smoke Suppression and Flame Retardancy of Epoxy Resin. *Compos. Sci. Technol.* **2020**, *189*, No. 108004.
- (40) Bi, H.; Zuo, X.; Liu, B. B.; He, D. M.; Bai, L.; Wang, W. Q.; Li, X.; Xiao, Z. Y.; Sun, K.; Song, Q. L.; Zang, Z. G.; Chen, J. Z. Multifunctional Organic Ammonium Salt-modified SnO<sub>2</sub> Nanoparticles toward Efficient and Stable Planar Perovskite Solar Cells. *J. Mater. Chem. A* **2021**, *9*, 3940–3951.
- (41) Liu, B. B.; Bi, H.; He, D. M.; Bai, L.; Wang, W. Q.; Yuan, H. K.; Song, Q. L.; Su, P. Y.; Zang, Z. G.; Zhou, T. W.; Chen, J. Z. Interfacial Defect Passivation and Stress Release via Multi-Active-Site Ligand Anchoring Enables Efficient and Stable Methylammonium-Free Perovskite Solar Cells. *ACS Energy Lett.* **2021**, *6*, 2526–2538.
- (42) Zhang, Z.; Baranwal, A. K.; Sahamir, S. R.; Kapil, G.; Sanehira, Y.; Chen, M. M.; Nishimura, K.; Ding, C.; Liu, D.; Li, H.; Li, Y. S.; Kamarudin, M. A.; Shen, Q.; Ripolles, T. S.; Bisquert, J.; Hayase, S. Large Grain Growth and Energy Alignment Optimization by Diethylammonium Iodide Substitution at A Site in Lead-Free Tin Halide Perovskite Solar Cells. *Sol. RRL* **2021**, *5*, No. 2100633.
- (43) Liu, Y. C.; Xu, Z.; Yang, Z.; Zhang, Y. X.; Cui, J.; He, Y. H.; Ye, H. C.; Zhao, K.; Su, H. M.; Lu, R.; Liu, M.; Kanatzidis, M. G.; Liu, S. Inch-Size 0D-Structured Lead-Free Perovskite Single Crystals for Highly Sensitive Stable X-Ray Imaging. *Matter* **2020**, *3*, 180–196.
- (44) Zhang, F.; Ye, S.; Zhang, H.; Zhou, F.; Hao, Y.; Cai, H.; Song, J.; Qu, J. Comprehensive Passivation Strategy for Achieving Inverted Perovskite Solar Cells with Efficiency Exceeding 23% by Trap Passivation and Ion Constraint. *Nano Energy* **2021**, *89*, No. 106370.
- (45) Ni, Z.; Bao, C.; Liu, Y.; Jiang, Q.; Wu, W. Q.; Chen, S.; Dai, X.; Chen, B.; Hartweg, B.; Yu, Z.; Holman, Z.; Huang, J. Resolving Spatial and Energetic Distributions of Trap States in Metal Halide Perovskite Solar Cells. *Science* **2020**, *367*, 1352–1358.
- (46) Kim, H. S.; Mora-Sero, I.; Gonzalez-Pedro, V.; Fabregat-Santiago, F.; Juarez-Perez, E. J.; Park, N. G.; Bisquert, J. Mechanism of Carrier Accumulation in Perovskite Thin-absorber Solar Cells. *Nat. Commun.* **2013**, *4*, 2242.
- (47) Guerrero, A.; Bisquert, J.; Garcia-Belmonte, G. Impedance Spectroscopy of Metal Halide Perovskite Solar Cells from the Perspective of Equivalent Circuits. *Chem. Rev.* **2021**, *121*, 14430–14484.
- (48) Ministry of Health of China Standardization Administration of China; *Standards for Drinking Water Quality*. Standards Press of China: China, 2006; Vol. GB 5749-2006.
- (49) Lv, M. Overview of Lead in Water Related Environmental Standards. In *China Science & Technology Panorama Magazine*; 2017; Vol. 6; pp 14–15.